

Machine learning boosting the discovery of porous metamaterials with an abnormal thermal transport property

Cite as: Appl. Phys. Lett. **122**, 144102 (2023); doi: [10.1063/5.0137665](https://doi.org/10.1063/5.0137665)

Submitted: 5 December 2022 · Accepted: 19 March 2023 ·

Published Online: 7 April 2023



View Online



Export Citation



CrossMark

Yu Yang,  Yunshan Zhao,^{a)}  and Lifa Zhang^{a)} 

AFFILIATIONS

Phonon Engineering Research Center of Jiangsu Province, Center for Quantum Transport and Thermal Energy Science, Institute of Physics Frontiers and Interdisciplinary Sciences, School of Physics and Technology, Nanjing Normal University, Nanjing 210023, China

Note: This paper is part of the APL Special Collection on Accelerate Materials Discovery and Phenomena.

^{a)}Author to whom correspondence should be addressed: phyzys@njnu.edu.cn and phyzlf@njnu.edu.cn

ABSTRACT

Normally, the introduction of porous structures into materials can tune their thermal conductivity, showing great applications in thermal management and thermoelectric energy harvesting. However, the ability of disorder changing the thermal conductivity of porous materials has seldom been explored. In this work, we show that an introduction of disorder into the macroscopic porous materials with a certain porosity can lead to a desired effective thermal conductivity over a large range, where an abnormal enhancement of $\sim 7.9\%$ and a normal reduction of $\sim 44\%$ at room temperature are predicted by the machine-learning-optimized algorithm. All of these theoretical calculation results are further verified by our experiments performed in the current work by using the steady-state thermal flux method. Moreover, when these periodic units are artificially connected, a structural anisotropy up to 40 is achieved, which can be further used to adjust the direction of the thermal flux in a well-controlled way. Our work provides an efficient and convenient approach for designing high-performance porous materials with specific thermal conductivity and high structural anisotropy for various applications in thermal management.

Published under an exclusive license by AIP Publishing. <https://doi.org/10.1063/5.0137665>

The efficient management of heat is essential and challenging for many fast-developing industries unprecedentedly in recent years, such as thermal dissipation in the nano-level chip,¹ thermal management in the new energy vehicle,² the low-carbon-oriented thermal energy recovery management,³ etc. A variety of strategies have been proposed recently to achieve high-performance thermal management in both macroscopic and microscopic thermal transport.^{4–6} On the microscopic scale, the idea of “phonon engineering” has been employed to achieve various interesting thermal control phenomena, such as phonon coherence,^{7–9} phonon localization,¹⁰ phonon devices,^{11,12} etc. Macroscopically, abundant thermal metamaterials, which are primary for designing the thermal conductivity of bulk materials, have been proposed and have great applications in various thermal functional devices.^{13–15} Among the emerging various metamaterials, porous materials are normally explored as a simple one with rich physical properties. For a homogeneous and symmetric porous material, called phononic crystals (PCs),¹⁶ the propagation of phonon wave in it will produce a phonon interference,^{17,18} leading to a large reduction ($\sim 10^2$ times reduction

compared to the bulk value) in its thermal conductivity,^{19–24} and, thus, PCs have potential applications in thermoelectrics.^{25,26}

An even disordered structure could be introduced into the porous materials, and it is expected that a further reduction in the thermal conductivity would be obtained in this way compared to that of the ordered structures.^{24,27–33} However, Maire *et al.* demonstrated that the disorder in low dimensional silicon-on-insulator wafer could lead to an abnormal enhancement in thermal conductivity at 4 K, which is inconsistent with the previous results.³⁴ The origin is attributed to the fact that the greater the disorder is, the cutoff frequency of the coherent phonons is shifted to the low frequency regime, resulting in the existence of more high-frequency phonons and a further enhancement in thermal conductivity. All the subsequent calculations obtained contradictory results until Wei *et al.* used a genetic algorithm to seek out several configurations, where the introduction of the disorder structures could, indeed, enhance the thermal conductivity at 300 K.³⁵ However, the physical mechanism here is that rather than the assumptions of the wave like behavior of phonon, the abnormal

enhancement in the thermal conductivity is attributed to the particle behavior of phonons, which is closely related to the special pore arrangement. Although these interesting works show the potential application of disordered porous metamaterials, they focus on the low temperature and on the micro- or nano-scale, and for the macroscopic materials that are more applicable at room temperature or even higher temperature conditions, there is a lack of study yet.^{36–38}

In this work, we demonstrate that in a macroscopic system, the thermal conductivity can be abnormally enhanced by introducing a suitable disorder. The configuration with abnormal enhancement ($\sim 7.9\%$) and the normal reduction ($\sim 44\%$) in the effective thermal conductivity (ETC) have been shown by using a multi-layer perceptron (MLP)^{39–49} and the particle swarm optimization (PSO)

algorithm.^{50–53} Unexpectedly, these two configurations are actually along the two directions of the same configuration with a structural anisotropy ratio around 2. An experimental measurement based on the steady thermal flux method is carried out to confirm the theoretical prediction. Moreover, by extending the configuration layer, a structure with an anisotropy ratio exceeding 40 is achieved, and the application of thermal control is further demonstrated in this study. Our work provides an effective way for the design of high-performance porous materials for thermal management applications.

A two-dimensional porous alumina sheet with a square side length of $a = 4$ m is employed in our study, as shown in Fig. 1(a). Periodic pores with radius $r = 0.3$ m are uniformly arranged along the x and y directions. The typical finite element method (FEM, Method

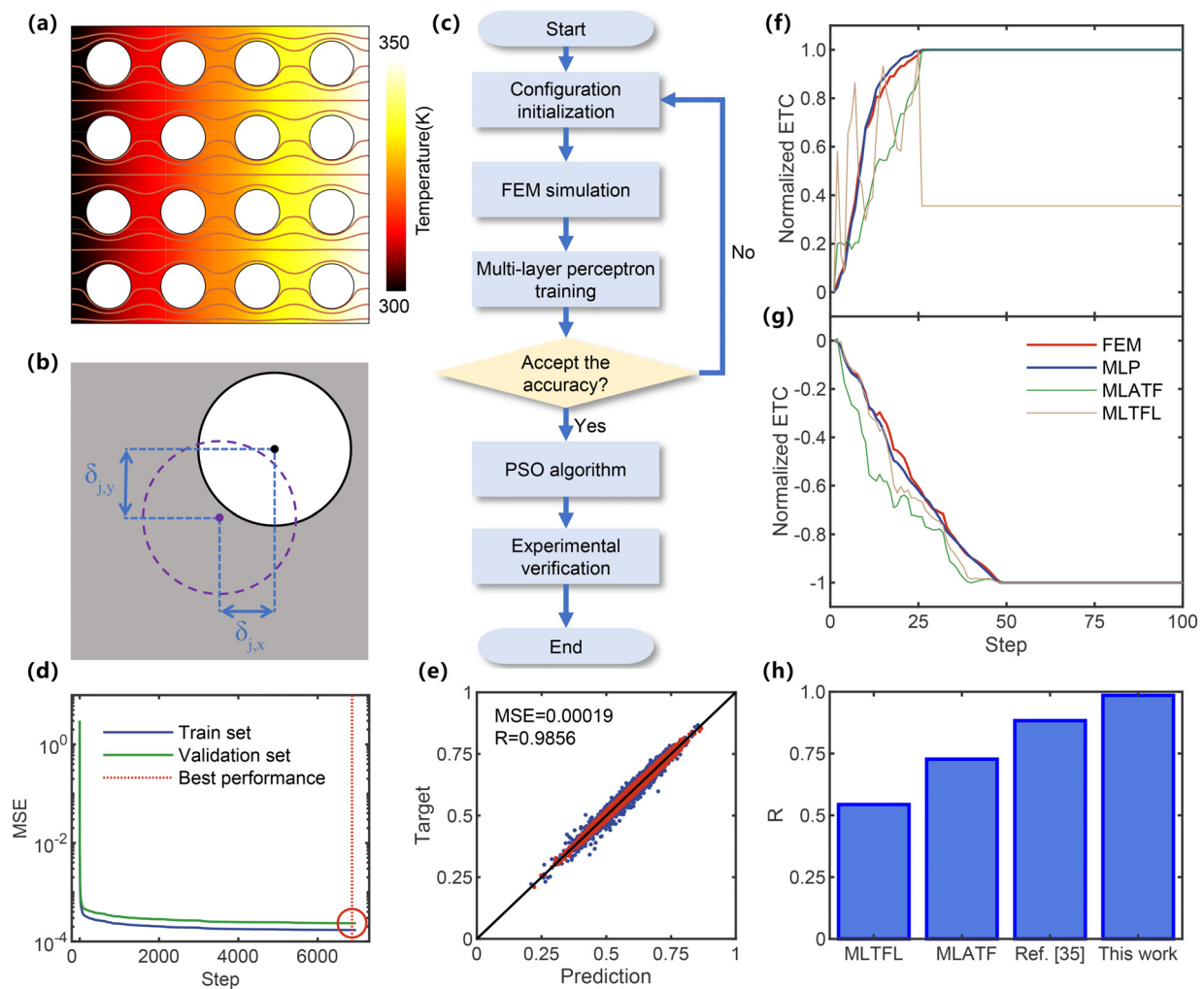


FIG. 1. Active learning, optimization, and performance comparison of MLP. (a) The temperature distribution and partial thermal flux line (brown curve) of the uniform arrangement configuration. (b) A schematic diagram of moving the pore to construct the disordered configuration. (c) A complete flow chart of the entire research. (d) The MSE of the training set and the validation set as two functions of the training step. The red circle marks the position of the optimal training performance. (e) The accurate ETC obtained by the FEM is a function of the predicted ETC by the MLP. The red scattered dots indicate the configuration with the lowest 90% absolute error, which implies that the remaining 10% configuration brings greater broadening. (f) and (g) The optimization process of the largest-ETC configuration and the smallest-ETC configuration by using the MLP and the PSO algorithm (blue curve). The red, green, and beige lines show the accurate value of the FEM, the predicted value of the MLATF method, and the predicted value of the MLTFL method for comparison, respectively. (h) The correlation coefficient histogram of the MLTFL method, MLATF method, artificial descriptor, and MLP.

S1) is employed to obtain the average thermal flux J of the entire porous material under the external thermal temperature difference ΔT . The effective thermal conductivity κ_e can be calculated by Fourier's law, as follows:

$$\kappa_e = \frac{J}{\Delta T}. \quad (1)$$

Then, the position of each pore is randomly adjusted to construct a disordered configuration dataset for the subsequent study. As shown in Fig. 1(b), the displacement of the j -th pore in the x and y directions is denoted by $\delta_{j,x}$ and $\delta_{j,y}$, respectively. We define the degree of disorder of the i -th configuration δ_i as the maximum value of $\delta_{j,x}$ and $\delta_{j,y}$. Initially, we investigate 2000 randomly generated configurations in different degrees of disorder, and their ETC is shown in Fig. S1. Different from that in the previous work, it is much convenient here to find the configurations with abnormal enhancement in ETC, especially for the high disorder case. The next question is why there is an abnormal enhancement in ETC at room temperature and at the macroscopic limit, and what is the limit for it. In order to better understand the calculation process, a complete flow chart is shown in Fig. 1(c).

Due to the fact that there are many parameters for each configuration, and that the complex coupling between these parameters together affects ETC, it is difficult to establish a direct function that accurately describes the configuration and its ETC. The multi-layer perceptron (MLP) is selected as the predictive model between the generation configuration and its ETC, considering its higher accuracy and greater universality than the previous artificial-guessed predictive models.^{39–42,44–46} Here, the four-layer MLP is optimized by the back-propagation method, and its structure is shown in Fig. S2 (the detailed introduction in Method S2). To achieve the high accuracy, 55 000 random configurations and 7000 training steps are performed. The overall training process is shown in Figs. 1(d) and S3. We use the following mean square error (MSE) and correlation coefficient (R) to evaluate the accuracy of MLP:

$$MSE = \frac{1}{n} \sum_{i=1}^n (y_i - \hat{y}_i)^2, \quad (2)$$

$$R = \frac{\sqrt{\sum_{i=1}^n (\hat{y}_i - \bar{y})^2}}{\sqrt{\sum_{i=1}^n (y_i - \bar{y})^2}}. \quad (3)$$

In Eqs. (2) and (3), y_i represents the accurate value by FEM, \hat{y}_i represents the predicted value by MLP, and \bar{y} represents the mean of y_i . The predicted ETC of the complete set based on the MLP is shown in Fig. 1(e), and the correlation coefficient R and the mean square error MSE of the MLP are 0.9856 and 1.9×10^{-4} , respectively. In particular, Figs. S4 and S5 show that the training set, the validation set, and the test set have a common high accuracy, implying that the issue of over-fitting does not exist in this highly accurate MLP.

The MLP well describes the relationship between configuration and its ETC, providing an opportunity to find the optimal disordered configuration. Since the candidate configurations are distributed in a continuous huge 32-dimensional space, which is quite intractable for the common optimization algorithm, the particle swarm optimization

(PSO) algorithm is employed in this work (Method S3). The 300 initial particles (configurations) are released in the high-dimensional parameter space, and then they keep moving toward the optimum state. Finally, around the 50th optimization step, the algorithm converges and shows a better disordered configuration, as shown in Figs. 1(f), 1(g), and S6. The schematic diagram of the configuration with the largest- and smallest-ETC obtained by the PSO is shown in the inset of Fig. 2. The largest-ETC is enhanced by 7.9% compared to that of the uniform arrangement, while the smallest-ETC is reduced by 44%. The relative change factor μ is defined as follows:

$$\mu = \frac{\kappa_r - \kappa_u}{\kappa_u}. \quad (4)$$

Here, κ_r and κ_u represent the ETC of the random configuration and the uniform arrangement configuration, respectively. By comparing the optimal configurations, the largest- and smallest-ETC are actually along the two directions of the same configuration, with a structural anisotropy ratio of about 2. In this paper, the anisotropy ratio γ is defined as follows:

$$\gamma = \frac{\kappa_{e,y}}{\kappa_{e,x}}. \quad (5)$$

Here, $\kappa_{e,x(or y)}$ represents the ETC along the x (or y) direction. One conclusion in Fig. S7 is that as the disorder become greater, the accompanied anisotropy increases quickly, which possibly has a significant application in thermal management^{36–38} and thermoelectric energy harvesting.⁵⁴ Compared with the previous work, the optimal

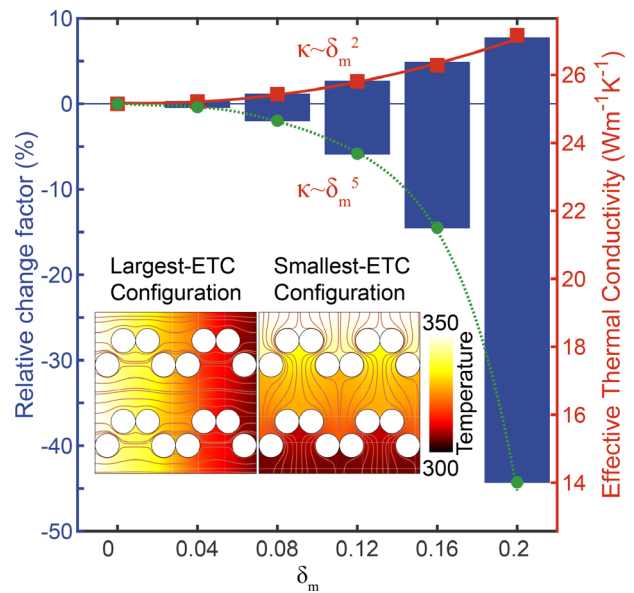


FIG. 2. The optimal disordered configuration in different degrees of disorder. The blue histogram shows the largest relative enhancement percentage and largest reduction percentage in different degrees of disorder. Red square and green circle scatters give the ETC of the largest- and smallest-ETC disordered configuration in different degrees of disorder. In the inset, we show the largest-ETC configuration and the smallest-ETC configuration in the disorder degree of 0.2, and the temperature distribution and uniformly spaced thermal flux lines are also shown in the inset figure.

configuration obtained by MLP and the PSO algorithm have a higher symmetry and regularity. Moreover, some fuzzy local structural characteristics of the optimal configuration shown in previous studies have been reproduced, extended, and further optimized here.^{34,35} In addition, we compare the performance of MLP and other artificial predictive models, such as mean local angle of thermal flux (MLATF),^{55,56} mean length of thermal flux line (MLTFL), and artificial predictive model,³⁵ as shown in Figs. 1(h), S8, and S9. The automatic search method based on a combination of MLP and PSO optimization will be more accurate and extendable in the designing of porous thermal metamaterials (detailed discussions in the [supplementary material](#) Method S4).

To verify our theoretical predictions, a system based on the steady-state thermal flux method is built up in a vacuum chamber, where the pressure lower than 10^{-6} mbar during measurement is provided to avoid the possible effects of thermal convection, thermal radiation, etc., and the detailed setup is shown in Figs. 3(a) and 3(b). The copper substrate and cooper sheet are served as the heater and the sink, respectively. The temperature gradient and thermal flux on the sample are obtained by two thermal sensors. The front and side view of the measurement system are shown in Figs. S10(a) and S10(b), respectively. The prepared porous materials are shown in Fig. S10(c),

and the details of the experimental measurements are shown in Method S5.

In the experiment, the polyimide thermal tapes with a relatively low thermal conductivity ($0.1\text{--}0.35\text{ W m}^{-1}\text{ K}^{-1}$)^{157,58} are used to improve the thermal contact between the thermal flux sensors and the sample. As shown in Fig. 3(c), the ETC of the whole system shows an apparently abnormal enhancement and normal reduction, verifying our theoretical prediction. In order to obtain the intrinsic thermal transport properties, the temperature difference cross-matching method (the details in the [supplementary material](#) Method S6) is used to eliminate the possible effect from the interface thermal resistance (ITR), thermal tape as well as the measurement system. Here, we define these effects as the effective ITR ($R_{\text{eff},i}$) as follows:

$$R_{\text{eff},i} = R_{\text{total thermal tap}} + 2R_{\text{thermal flux sensor}} + R_{\text{total interface}}, \quad (6)$$

where $R_{\text{total thermal tap}}$, $R_{\text{thermal flux sensor}}$, and $R_{\text{total interface}}$ represent the resistance of the total thermal tap, thermal flux sensor, and the total interface, respectively.

Moreover, an identical structure, including the thermal tape, the thermal flow direction regulator, the cooper heater, and the copper sheet, is established by using the FEM to achieve the temperature difference cross-matching method. In Fig. 3(d), it is apparently observed

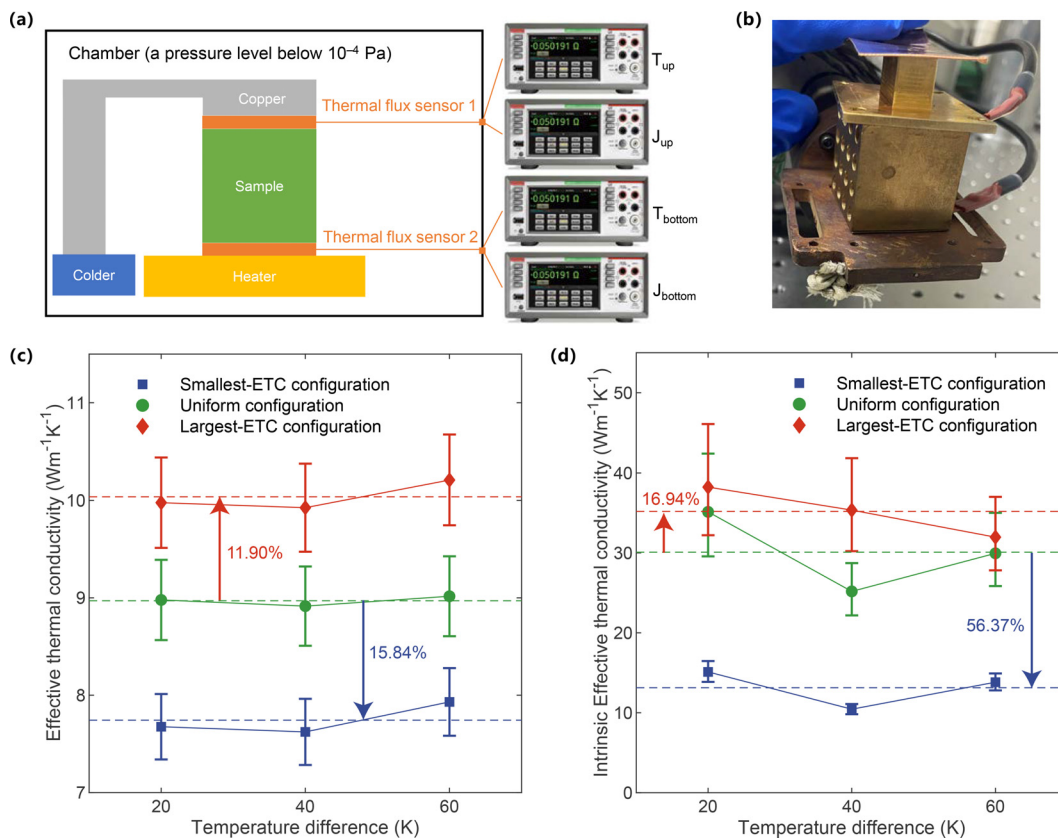


FIG. 3. The schematic diagram and the result of experimentally measuring the optimal disordered configuration. (a) A schematic diagram of experimentally measuring the ETC of the optimal disordered configuration. (b) The front view of the experimental measurement system. (c) and (d) The experimental measurement results of the ETC and the intrinsic ETC of the largest-ETC configuration (red diamond), uniform arrangement configuration (green circle), and smallest-ETC configuration (blue square) under different temperature differences. The dotted line gives the mean of the ETC and the intrinsic ETC in the different temperature difference cases.

that once considering the $R_{\text{eff},i}$, the intrinsic ETC is well in agreement with the theoretical prediction, and a more obviously abnormal enhancement and a normal reduction in intrinsic ETC have been observed. The relative change factor μ after considering $R_{\text{eff},i}$ is shown in Fig. S11(e), which is well consistent with the theoretical prediction as well. The structure with an anisotropy ratio γ as high as 1.62, as predicated by our calculation, is verified in the experiment performed in our study.

The mechanism behind the abnormal enhancement and the normal reduction in the intrinsic ETC is further discussed here. In Eqs. (S6) and (S7), $\nabla T(x, y)$ gives the thermal flux direction of the entire material. Similar to the electric field line, each thermal flux line is a separate contribution to the entire material, and the overall ETC is summation of all individual thermal flux lines. The mathematical form is as follows:

$$\frac{1}{R_e} = \sum_i \frac{1}{R_i} = \sum_i \frac{S_i}{\rho l_i}. \quad (7)$$

In Eq. (7), i represents i th separate thermal flux line, and l_i and S_i represent the length and cross-sectional area of the i th thermal flux line, respectively. If the thermal flux lines in the porous material are straight and slightly curved, the local angle of thermal flux would decrease, leading to a larger ETC. In Fig. S8 for the smallest-ETC configuration, there are some large bright spots and bright bands along the local angle of thermal flux, meaning a significantly larger local angle of thermal flux than other configurations as well as a smaller ETC. In the macroscopic systems, the abnormal enhancement in thermal

conductivity could not arise from the wave-like behavior of phonons³⁴ but from the particle-like behavior of phonons,^{9,35} which is closely related to the special geometric factor.

Furthermore, considering the fact that large number of pores and even complex porous structures are typically employed in the practical applications, the porous configurations with more periodic units, different number of layers, and blocks are constructed as shown in Fig. S12. As the block becomes larger, the structural anisotropy ratio also increases rapidly, which could increase to 40 when the number of units in the block is 10 and the structure ratio is about 0.5, as shown in Fig. 4(a). Here, the structure ratio is defined as the number of layers divided by the maximum number of layers, and the corresponding normalized thermal flux is shown in Fig. S13(a). Such a high structural anisotropic ratio would be beneficial to improve the overall anisotropic ratio, even though the material itself has a lattice anisotropy. The overall anisotropic ratio, including the combined effects of the structural anisotropic ratio and material anisotropic ratio, could be significantly improved once considering the optimal structure ratio for each block as shown in Figs. 4(b) and S13(b). It is worth noting that the structure anisotropy dominates in the overall anisotropy, as shown in Fig. S13(c). Therefore, it is desirable and useful to use this high structural anisotropy for thermal control. In Fig. 4(c), an example of using a porous structure with a highly thermal anisotropic ratio to heat an NNU-shaped region is shown, which includes various forms of management of thermal fluxes. More importantly, the structural anisotropy of such porous structures does not change with the scaling of the smallest structural unit [Fig. S13(d)], so the design of such highly

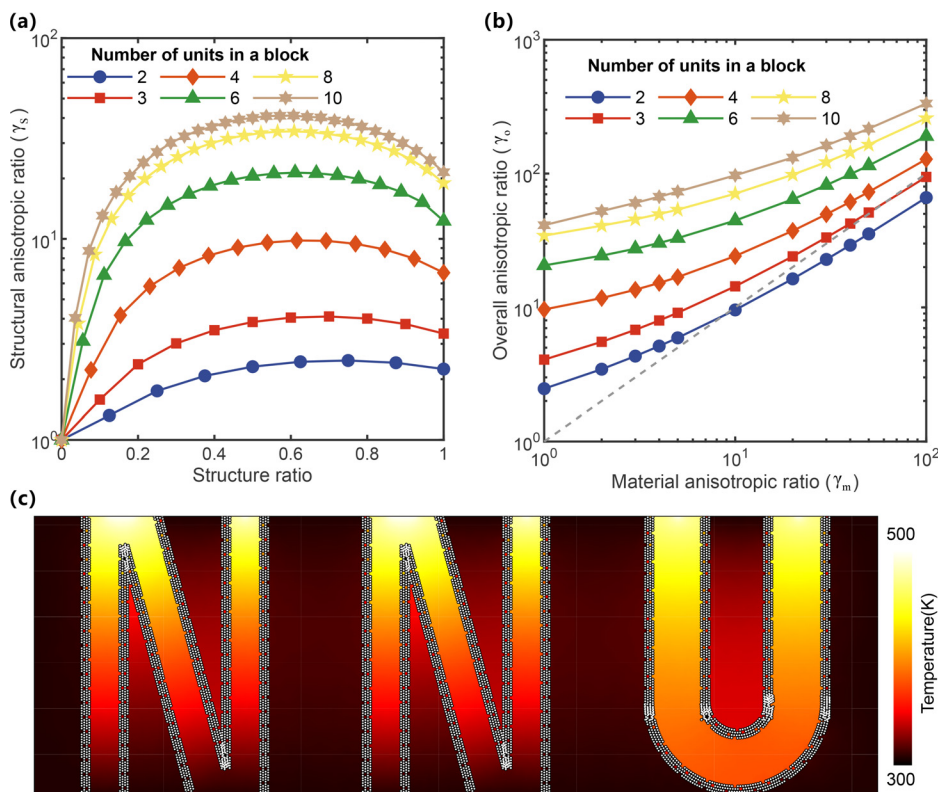


FIG. 4. Anisotropy and application of porous materials with the extended block. (a) The structural anisotropic ratio as a function of structure ratio for different number of units in a block. (b) The overall anisotropic ratio as a function of material anisotropic ratio for different number of units in a block. Here, the gray dashed line indicates that the material anisotropy is equal to the overall anisotropy. (c) An application example of using high-anisotropic porous materials to redirect the thermal flux and an artificially NNU is designed.

anisotropic porous materials would be flexible and has potential applications in thermal control and thermal management.

In summary, we study the effect of disorder on the ETC of porous materials. An optimal disorder configuration with the largest abnormal enhancement in ETC of the porous material is shown at the macroscopic limit and at room temperature, and a steady-state thermal flux method measurement system is used to verify these theoretical calculations results. According to our study, the abnormal enhancement in ETC does not come from the contribution of the coherent phonons, while is closely related to the geometric arrangement of the pores in the configuration, and even exists in the system with a high interface thermal resistance. The systematic optimization method we proposed in this work can be extended to the system with different shapes of pores and different porosity. Moreover, a combination of a series of basic units in the block will lead to an ultra-high structural anisotropy to obtain the function of redirecting, splitting, and turning the thermal flux, which will be of great significance for advancing the application of porous metamaterials to achieve the flexible and high-performance thermal management and control.

See the [supplementary material](#) for the details.

This work was supported by the National Natural Science Foundation of China (Grants Nos. 11975125, 11890703, and 12204244) and the Natural Science Foundation of Jiangsu Province (Grant No. BK20210556). Z.Y.S. acknowledges support from the Jiangsu Specially-Appointed Professor Program. Y.Y. acknowledges support from the Postgraduate Research & Practice Innovation Program of Jiangsu Province (Grant No. KYCX22 1539).

AUTHOR DECLARATIONS

Conflict of Interest

The authors have no conflicts to disclose.

Author Contributions

Yu Yang: Conceptualization (equal); Data curation (equal); Formal analysis (equal); Writing – original draft (equal); Writing – review & editing (equal). **Yunshan Zhao:** Conceptualization (equal); Data curation (equal); Funding acquisition (equal); Project administration (equal); Resources (equal); Supervision (equal); Validation (equal); Writing – original draft (equal); Writing – review & editing (equal). **Lifa Zhang:** Conceptualization (equal); Data curation (equal); Investigation (equal); Resources (equal); Supervision (equal); Validation (equal); Writing – original draft (equal); Writing – review & editing (equal).

DATA AVAILABILITY

The data that support the findings of this study are available within the article and its [supplementary material](#).

REFERENCES

- M. M. Waldrop, *Nature* **530**, 144 (2016).
- Q. Wang, B. Jiang, B. Li, and Y. Yan, *Renewable Sustainable Energy Rev.* **64**, 106 (2016).
- Z. Liu, *Nature* **500**, 143 (2013).
- Y. Li, W. Li, T. Han, X. Zheng, J. Li, and B. Li, *Nat. Rev. Mater.* **6**, 488 (2021).
- S. R. Sklan and B. Li, *Nat. Sci. Rev.* **5**, 138 (2018).
- N. Li, J. Ren, L. Wang, G. Zhang, P. Hänggi, and B. Li, *Rev. Mod. Phys.* **84**, 1045 (2012).
- M. N. Luckyanova, J. Garg, K. Esfarjani, A. Jandl, M. T. Bulsara, A. J. Schmidt, A. J. Minnich, S. Chen, M. S. Dresselhaus, Z. Ren, E. A. Fitzgerald, and C. Gang, *Science* **338**, 936 (2012).
- J. K. Yu, S. Mitrovic, D. Tham, J. Varghes, and J. R. Heath, *Nat. Nanotechnol.* **5**, 718 (2010).
- J. Chen, D. Pan, X. Wang, N. Yang, J. Zhu, S. A. Yang, and G. Zhang, *Nature Mater.* **14**, 667–674 (2015).
- B. L. Davis and M. I. Hussein, *Phys. Rev. Lett.* **112**, 055505 (2014).
- B. Li, L. Wang, and G. Casati, *Phys. Rev. Lett.* **93**, 184301 (2004).
- B. Li, L. Wang, and G. Casati, *Appl. Phys. Lett.* **88**, 143501 (2006).
- C. Z. Fan, Y. Gao, and J. P. Huang, *Appl. Phys. Lett.* **92**, 251907 (2008).
- R. Schittny, M. Kadic, S. Guenneau, and M. Wegener, *Phys. Rev. Lett.* **110**, 195901 (2013).
- S. Narayana and Y. Sato, *Phys. Rev. Lett.* **108**, 214303 (2012).
- T. Vasileiadis, J. Varghese, V. Babacic, J. Gomis-Bresco, D. N. Urrios, and B. Graczykowski, *J. Appl. Phys.* **129**, 160901 (2021).
- M. Maldovan, *Phys. Rev. Lett.* **110**, 025902 (2013).
- M. Maldovan, *Nature Nano.* **5**, 718–721 (2010).
- D. Song and G. Chen, *Appl. Phys. Lett.* **84**, 687 (2004).
- P. E. Hopkins, C. M. Reinke, M. F. Su, R. H. Olsson III, E. A. Shaner, Z. C. Leseman, J. R. Serrano, L. M. Phinney, and I. El-kady, *Nano Lett.* **11**, 107 (2011).
- L. Yang, N. Yang, and B. Li, *Nano Lett.* **14**, 1734 (2014).
- S. Alaie, D. F. Goettler, M. Su, Z. C. Leseman, C. M. Reinke, and I. El-Kady, *Nat. Commun.* **6**, 7228 (2015).
- T. Feng and X. Ruan, *Carbon* **101**, 107 (2016).
- Y. Zhao, L. Yang, L. Kong, M. H. Nai, D. Liu, J. Wu, Y. Liu, S. Y. Chiam, W. K. Chim, C. T. Lim, B. Li, J. T. L. Thong, and K. Hippalgaonkar, *Adv. Funct. Mater.* **27**, 1702824 (2017).
- J. H. Lee, G. A. Galli, and J. C. Grossman, *Nano Lett.* **8**, 3750 (2008).
- J. Tang, H. T. Wang, D. H. Lee, M. Fardy, Z. Huo, T. P. Russell, and P. Yang, *Nano Lett.* **10**, 4279 (2010).
- R. Anufriev, A. Ramiere, J. Maire, and M. Nomura, *Nat. Commun.* **8**, 15505 (2017).
- M. Kasprzak, M. Sledzinska, K. Zaleski, I. Iatsunskyi, F. Alzina, S. Volz, C. M. S. Torres, and B. Graczykowski, *Nano Energy* **78**, 105261 (2020).
- M. R. Wagner, B. Graczykowski, J. S. Reparaz, A. E. Sachat, M. Sledzinska, F. Alzina, and C. M. S. Torres, *Nano Lett.* **16**, 5661 (2016).
- J. Oh, H. Yoo, J. Choi, J. Y. Kim, D. S. Lee, M. J. Kim, J. C. Lee, W. N. Kim, J. C. Grossman, J. H. Park, S. S. Lee, H. Kim, and J. G. Son, *Nano Energy* **35**, 26 (2017).
- S. Hu, Z. Zhang, P. Jiang, J. Chen, S. Volz, M. Nomura, and B. Li, *J. Phys. Chem. Lett.* **9**, 3959 (2018).
- S. Hu, Z. Zhang, P. Jiang, W. Ren, C. Yu, J. Shiomi, and J. Chen, *Nanoscale* **11**, 11839 (2019).
- M. Sledzinska, B. Graczykowski, F. Alzina, U. Melia, K. Termentzidis, D. Lacroix, and C. M. S. Torres, *Nanotechnology* **30**, 265401 (2019).
- J. Maire, R. Anufriev, R. Yanagisawa, A. Ramiere, S. Volz, and M. Nomura, *Sci. Adv.* **3**, e1700027 (2017).
- H. Wei, H. Bao, and X. Ruan, *Nano Energy* **71**, 104619 (2020).
- Y. F. Huang, Z. G. Wang, H. M. Yin, J. Z. Xu, Y. Chen, J. Lei, L. Zhu, F. Gong, and Z. M. Li, *ACS Appl. Nano Mater.* **1**, 3312 (2018).
- Z. G. Wang, W. Liu, Y. H. Liu, Y. Ren, Y. P. Li, L. Zhou, J. Z. Xu, J. Lei, and Z. M. Li, *Composites, Part B* **180**, 107569 (2020).
- I. I. Smalyukh, *Adv. Mater.* **33**, 2001228 (2021).
- R. Ramprasad, R. Batra, G. Pilania, A. Mannodi-Kanakkithodi, and C. Kim, *npj Comput. Mater.* **3**, 54 (2017).
- H. Zhang, K. Hippalgaonkar, T. Buonassisi, O. M. Løvvik, E. Sagvolden, and D. Ding, *ES Energy Environ.* **2**, 1–8 (2018).
- X. Wan, W. Feng, Y. Wang, H. Wang, X. Zhang, C. Deng, and N. Yang, *Nano Lett.* **19**, 3387 (2019).
- T. Zhan, L. Fang, and Y. Xu, *Sci. Rep.* **7**, 7109 (2017).
- Y. J. Wu, L. Fang, and Y. Xu, *npj Comput. Mater.* **5**, 56 (2019).

- ⁴⁴H. Wei, S. Zhao, Q. Rong, and H. Bao, *Int. J. Heat Mass Transfer* **127**, 908 (2018).
- ⁴⁵Q. Rong, H. Wei, X. Huang, and H. Bao, *Compos. Sci. Technol.* **184**, 107861 (2019).
- ⁴⁶H. Miyazaki, T. Tamura, M. Mikami, K. Watanabe, N. Ide, O. M. Ozkendir, and Y. Nishino, *Sci. Rep.* **11**, 13410 (2021).
- ⁴⁷Y. Saito, K. Shin, K. Terayama, S. Desai, M. Onga, Y. Nakagawa, Y. M. Itahashi, Y. Iwasa, M. Yamada, and K. Tsuda, *NPJ Comput. Mater.* **5**, 124 (2019).
- ⁴⁸R. Hu, S. Iwamoto, L. Feng, S. Ju, S. Hu, M. Ohnishi, N. Nagai, K. Hirakawa, and J. Shiomi, *Phys. Rev. X* **10**, 021050 (2020).
- ⁴⁹P. R. Chowdhury, C. Reynolds, A. Garrett, T. Feng, S. P. Adiga, and X. Ruan, *Nano Energy* **69**, 104428 (2020).
- ⁵⁰J. Kennedy and R. Eberhart, in Proceedings of ICNN'95—International Conference on Neural Networks, 1995, Vol. 4.
- ⁵¹K. E. Parsopoulos and M. N. Vrahatis, *Nat. Comput.* **1**, 235 (2002).
- ⁵²M. Weiel, M. Götz, A. Klein, D. Coquelin, R. Floca, and A. Schug, *Nat. Mach. Intell.* **3**, 727 (2021).
- ⁵³M. S. Alvarez-Alvarado, F. E. Alban-Chacón, E. A. Lamilla-Rubio, C. D. Rodríguez-Gallegos, and W. Velásquez, *Sci. Rep.* **11**, 11655 (2021).
- ⁵⁴Y. Xiao and Q. Hao, *Int. J. Heat Mass Transfer* **170**, 120944 (2021).
- ⁵⁵G. H. Tang, C. Bi, and B. Fu, *J. Appl. Phys.* **114**, 184302 (2013).
- ⁵⁶B. Fu, G. H. Tang, and C. Bi, *J. Appl. Phys.* **116**, 124310 (2014).
- ⁵⁷T. L. Li and S. L. C. Hsu, *J. Phys. Chem. B* **114**, 6825 (2010).
- ⁵⁸T. Wang, M. Wang, L. Fu, Z. Duan, Y. Chen, X. Hou, Y. Wu, S. Li, L. Guo, R. Kang, N. Jiang, and J. Yu, *Sci. Rep.* **8**, 1557 (2018).